Check for updates

A wireless haptic interface for programmable patterns of touch across large areas of the skin

Yei Hwan Jung[1,9], Jae-Young Yoo[2,9], Abraham Vázquez-Guardado[2,9], Jae-Hwan Kim[2,9], Jin-Tae Kim[2,9], Haiwen Luan[2], Minsu Park[2], Jaeman Lim[1,2], Hee-Sup Shin[2], Chun-Ju Su[2], Robert Schloen[2], Jacob Trueb[2], Raudel Avila[3], Jan-Kai Chang[2], Da Som Yang[2], Yoonseok Park[2], Hanjun Ryu[2], Hong-Joon Yoon[2], Geumbee Lee[2], Hyoyeong Jeong[2], Jong Uk Kim[2], Aadeel Akhtar[4], Jesse Cornman[4], Tae-il Kim[5], Yonggang Huang[3,6,7] and John A. Rogers[2,3,6,8 ✉]

Haptic interfaces can be used to add sensations of touch to virtual and augmented reality experiences. Soft, flexible devices that deliver spatiotemporal patterns of touch across the body, potentially with full-body coverage, are of particular interest for a range of applications in medicine, sports and gaming. Here we report a wireless haptic interface of this type, with the ability to display vibro-tactile patterns across large areas of the skin in single units or through a wirelessly coordinated collection of them. The lightweight and flexible designs of these systems incorporate arrays of vibro-haptic actuators at a density of 0.73 actuators per square centimetre, which exceeds the two-point discrimination threshold for mechanical sensation on the skin across nearly all the regions of the body except the hands and face. A range of vibrant sensations and information content can be passed to mechanoreceptors in the skin via time-dependent patterns and amplitudes of actuation controlled through the pressure-sensitive touchscreens of smart devices, in real-time with negligible latency. We show that this technology can be used to convey navigation instructions, to translate musical tracks into tactile patterns and to support sensory replacement feedback for the control of robotic prosthetics.

Haptic interfaces that provide cutaneous sensations allow humans to interact with computer systems and other types of machine through the sensation of touch[1–3]. Displaying tactile images on the skin can enhance virtual or augmented reality experiences beyond those that are supported by visual and auditory inputs alone[4–8]. Such interfaces have potential applications in education, training, medicine and rehabilitation, as well as consumer-oriented uses in gaming, entertainment and social media. Haptic feedback delivered in real time at relevant parts of the anatomy could, for instance, accelerate the training of proper sequences of movements in sports, manual work, military exercises, surgical operations and physical rehabilitation. Such interfaces could also be of use in sensory substitution for individuals with sensory impairments[9,10]. In the case of amputees, for instance, tactile stimuli delivered to the skin of residual limbs could facilitate the control of robotic prosthetics instrumented with sensors.

Haptic interfaces for hands and fingers use glove-type interfaces that deliver touch sensations in the form of programmable patterns of vibration and/or force, improving hand-to-hand or hand-to-object interactions[11–14]. Classes of haptic interfaces that are deployed across large areas of the skin, including the arms, legs, chest and back, can provide additional forms of sensations that occur during scenarios associated with complex tasks and with activities of daily life[15–19]. Conventional devices designed for such purposes are, however,

limited in their usability due to bulky and heavy form factors that prevent comfortable interfaces, fine spatiotemporal resolutions and/or large-area coverages, with hardwired connections that create complications and impede ordinary motions[20–22].

We recently reported a skin-integrated, wireless haptic interface technology that resolves many of these issues through the integration of arrays of small vibro-tactile actuators with stretchable control electronics, wireless power delivery schemes and wireless communication approaches[23]. The resulting platforms allow real-time, programmable patterns of haptic stimuli to be delivered across various locations of the body through touchscreens and other computer interfaces. Even these systems are, however, limited by a number of factors: short-range operating distances constrained by near-field power transfer and communication protocols (~50 cm), relatively large actuators (18 mm in diameter) at large separations (21 mm), high power consumption, non-ideal physical weight characteristics for mounting on the skin (~130 g in total) and an inability to program control over the strength of the haptic sensation.

In this Article, we report a lightweight, flexible technology that can display vibro-tactile patterns across large areas of the skin in single units or through a wirelessly coordinated collection of them. Compared with our previous approach, the technology offers a reduction in the size (by a factor of ~2) and weight (by a factor of ~5) of the overall system. It increases the density of the actuator

[1]Department of Electronic Engineering, Hanyang University, Seoul, Republic of Korea. [2]Querrey Simpson Institute for Bioelectronics, Northwestern University, Evanston, IL, USA. [3]Department of Mechanical Engineering, Northwestern University, Evanston, IL, USA. [4]PSYONIC, Champaign, IL, USA. [5]School of Chemical Engineering, Sungkyunkwan University (SKKU), Suwon, Republic of Korea. [6]Department of Materials Science and Engineering, Northwestern University, Evanston, IL, USA. [7]Department of Civil and Environmental Engineering, Northwestern University, Evanston, IL, USA. [8]Departments of Biomedical Engineering, Neurological Surgery, Chemistry, and Electrical and Computer Engineering, Northwestern University, Evanston, IL, USA. [9]These authors contributed equally: Yei Hwan Jung, Jae-Young Yoo, Abraham Vázquez-Guardado, Jae-Hwan Kim, Jin-Tae Kim. ✉e-mail: jrogers@northwestern.edu
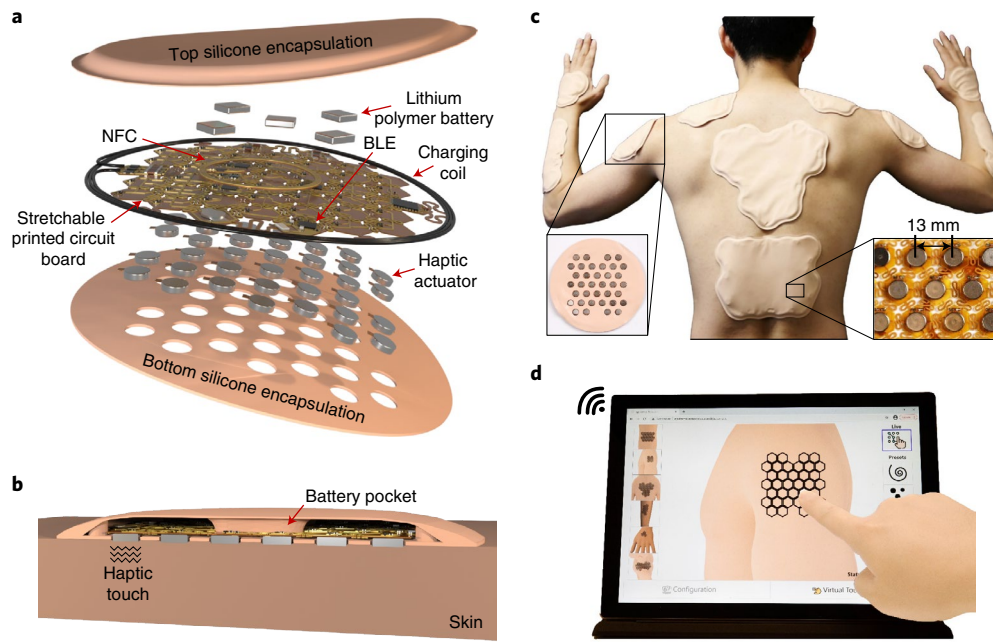
Fig. 1 | Structural designs, mechanical interfaces to the skin and touchscreen control system. a, Exploded-view schematic illustration of the electronic components, battery bank, vibrohaptic actuators and encapsulation structures. **b,** Cross-sectional schematic illustration of the device interfaced on the skin. The bottom encapsulation layer encloses the electronics and exposes the actuators through circular holes, allowing for direct contact between the skin and actuators. **c,** Photograph of haptic interfaces in various forms designed to fit the anatomical structures of different skin locations. **d,** Photograph of a GUI that allows the user to control individual actuators in real-time, with minimal latency, via a touchscreen on a computer or mobile device or to activate preprogrammed spatiotemporal patterns of actuation, both at the level of a given haptic interface or across a wirelessly coordinated collection of them at different locations of the body.

array (diameter of 7 mm and a pitch of 14 mm), to meet or exceed two-point discrimination thresholds across nearly all large-area regions of the body. It provides multi-modal actuators that improve the strength and power efficiency of haptic engagement. It extends the wireless operating distances (by a factor of ~20), and offers options in both battery and battery-free operation. It provides real-time control of the strength of haptic actuation, programmed through software or through pressure-sensitive touchscreens, and offers options in fast operation based on feedback from separate, wirelessly interfaced networks of sensors. A graphical user interface (GUI) identifiable by a uniform resource locator enables direct access via the Internet.

Our approach provides a realistic translation of sight, sound, pressure and other forms of information obtained from separate sensors into haptic forms of interaction over large areas of the skin. We illustrate the capabilities of the system by using it to display map directions for road navigation, translate musical tracks at high tempo into sensible tactile patterns and reconstruct tactile sensations for amputees through sensory replacement based on sensorized robotic prosthetics.

System architecture

Mimicking natural sensations of touch requires arrays of high-speed, independently controlled actuators distributed at relevant densities across the skin at anatomical locations that address application requirements. The focus here is on platforms that can address large areas of regions of the body beyond the fingertips. Figure 1 provides an overview of the architecture of a representative system. The device shown in Fig. 1a supports an array of 36 independently addressable actuators at a pitch of 13 mm (0.73 actuators per square centimetre) to allow spatiotemporal modulation at resolutions that meet or exceed the requirements based on two-point discrimination tests for the full engagement of mechanoreceptors

in the skin across nearly all the regions of the body except for the hands and face[24]. Specifically, although the skin associated with the face and hands offers the finest two-point discrimination resolution in the range of 2–4 mm, regions such as the upper arm, thigh, back and stomach support resolution in the range of ~40 mm due to the comparatively sparse distributions of receptors[15]. Unlike previously reported systems of this general type, the actuators incorporate brush-type eccentric rotating mass (ERM) vibration motors, each with a diameter of 7 mm, thickness of 2 mm and mass of 0.3 g, capable of generating maximum vibrational acceleration of 1.1G for a 100 g mass load, where 1 G is equal to the acceleration from gravity, in motions that involve both in-plane and out-of-plane displacements. Such accelerations can be reached with direct-current (d.c.) voltages, as a non-symmetric mass attached to the shaft of the motor rotates to produce an asymmetric centripetal force. At high revolutions per minute (r.p.m.) the resulting displacements appear on the skin as vibratory forms of actuation. Increases in the r.p.m. follow from increases in the applied voltage and consequent increases in both forces and displacements. As described subsequently, when attached directly to the skin, the large displacements (~10^2 μm) induced by ERM actuators both in the normal and shear directions lead to robust perception not only in sensitive areas of the skin but also in regions such as the arms and abdomen where the densities of mechanoreceptors is sparse and displacements in the range of ~10–100 μm are required for stimulation (Supplementary Table 1).

A double-sided flexible printed circuit board (FPCB) supports the actuators and associated control circuits, a small-scale FPCB for near-field communication (NFC), a charging coil and a lithium-ion polymer battery bank. Two thin layers of a soft, stretchable silicone elastomer form an encapsulating structure. The entire system weighs 33.68 g. A related battery-free embodiment replaces the batteries with a receiver and intermediate coil designed to wirelessly receive power via magnetic inductive coupling to a separate transmission

coil, which reduces the weight to 28.63 g. In both cases, the design and integration schemes exploit concepts in stretchable electronics, largely implemented with commercial components. The result is a scalable, compliant system capable of gentle mounting onto various curved surfaces of the body without discomfort[25,26].

Specifically, the overall layout of the main FPCB provides stretchability across a large area of the system through an array of hexagonal islands that physically and electrically connect together via serpentine-shaped structures with layouts optimized by finite element analysis of the mechanics. Each island supports a single actuator and associated driver circuit, mechanically isolated via serpentines that provide electrical interfaces to the main power source and control unit through six traces that emerge from the perimeter edges. The results of the finite element analysis indicate that the maximum effective strain in the copper remains below the yield strain (0.3%) during stretching, bending and twisting across ranges of motion relevant to mounting on large surfaces of the body (Supplementary Fig. 1).

The actuators receive power and control signals from surrounding islands that support the main electronic sub-systems, including (1) the power supply circuits with capabilities for battery-free operation of up to four actuators simultaneously over an operating range of several tens of centimetres from a transmission antenna or for battery-powered operation of all the 36 actuators simultaneously with an operating range limited only by the Bluetooth low-energy (BLE) interface (several metres or more); (2) a control unit with a port expander integrated circuit (IC) for control of the complete array; and (3) wireless systems that incorporate an NFC interface for turning the system on and off and a Bluetooth platform that controls the actuators in real time via wireless signals from an external, BLE-enabled device. All the components reside on the main FPCB except for the NFC tag, which is mounted on a separate, small FPCB that interfaces to the main board through a board-to-board connector. An inductive loop coil surrounds the entire system in the battery-free embodiment, for wireless inductive power harvesting from a transmission antenna. The battery-powered version uses five rechargeable 45 mAh lithium-ion polymer cells that reside inside air pockets formed in the inner part of the top silicone encapsulation layer (thickness, 0.4 mm; Supplementary Fig. 2a,b shows the images). In both cases, the bottom silicone encapsulation layer incorporates circular openings to expose the actuators for direct contact with and enhanced mechanical coupling to the skin (Fig. 1b) (The battery-free version uses a thin silicone layer for top encapsulation, without the air pockets (Supplementary Fig. 2c,d)). A disposable, doubled-sided silicone adhesive, also with circular openings, on the bottom silicone encapsulation layer secures the system to the skin. The presence of modest amounts of sweat does not decrease the adhesion strength (Supplementary Fig. 3).

Custom designs facilitate natural coverage across targeted body parts. The largest device described here includes 147 actuators in a shape configured to the interface with the back. This platform and others can be formed most easily using a strategy based on the assembly of small actuator arrays as prefabricated building blocks, described subsequently. Figure 1c shows different designs configured to conform to additional anatomical locations, including the shoulder, lower arm, dorsal hand, upper back and lumbar. Figure 1d highlights a GUI that allows a user to manipulate the haptic actuators via a BLE-enabled device with a touchscreen. The user can select from multiple skin-integrated haptic interfaces attached to different regions of the body, manipulate the full collection of actuators in real time and/or send preprogrammed spatiotemporal patterns of actuation to selected interfaces.

Circuit designs and operating principles

Figure 2a presents circuit and block diagrams that describe the operational organization and wireless connection to an external control system. A microcontroller that uses custom firmware provides logic to control the operation state of each actuator. Port expanders, interfaced via a serial communication protocol (I²C), support modular expansion options via 16 general-purpose input/output (GPI/O) pinouts per expander. The microcontroller generates digital pulse-width-modulated (PWM) signals with amplitude-shift keying (ASK) modulation to address any actuator in the array at a programmable frequency and duty cycle. These PWM signals result in smooth changes in the speed of the motors within the ERMs, where the inductances and resistances of the windings form low-pass analogue filters. This scheme controls the effective intensity of the haptic sensation through the duty cycle of the input. The microcontroller and port expander can deliver d.c. currents of up to 40 and 25 mA at each GPI/O, respectively, insufficient to drive a single ERM (48 mA). Metal–oxide–semiconductor field-effect transistors address these power requirements by acting as power-switching elements to drive the ERMs through direct interfaces to the regulated power source (for example, a battery bank or a wireless power-harvesting unit). A pull-down resistor (10 kΩ) that connects from the gate of the transistor to a ground node ensures a complete off state for each ERM by preventing any parasitic accumulation of charge. Another resistor (1 kΩ) connects from the gate to the GPI/O to limit the switching current. A 100 pF capacitor in parallel with the ERM suppresses high-frequency electromagnetic wideband noise generated by the motor. Additionally, a diode placed in parallel with the ERM protects the transistor against voltage spikes that can occur across the motor during periods of abrupt decreases in driving current.

The battery-free embodiment uses a receiver coil (silicone-coated wire, 26 gauge) that surrounds the board to wirelessly harvest power from a transmission antenna (Supplementary Fig. 4a). This coil offers superior levels of mechanical flexibility and quality factors compared with otherwise similar coils formed on the FPCB (Supplementary Fig. 4b,c). The maximum harvested power at the output of a rectifier that follows this coil is 1.8 W for an input power of 8.0 W at the transmission antenna (Supplementary Fig. 4d). An intermediate coil can be included to enhance the harvested power for long-range operation (Supplementary Fig. 4e). With this configuration, the harvested power is 700 mW at a distance of 50 cm from the transmission antenna, when the intermediate coil is at a position 10 cm away from the device (Supplementary Fig. 4f). Such power levels can activate the entire system and simultaneously operate up to four actuators at full power.

The computed specific absorption rate on the surface of the skin of a human torso as the point of attachment for a haptic interface during operation with an external radio-frequency (RF) transmission antenna (33.8 cm × 31.8 cm) transmitting 12 W of power 10 cm away from the torso at 13.56 MHz is 0.0142 W kg⁻¹, which is substantially less than the safety exposure limit outlined by the Federal Communications Commission (47 CFR Part 1.1310 and 15)[27] of 0.0800 W kg⁻¹ (Supplementary Fig. 5).

The system incorporates a microprocessor (Arm Cortex-M3) that contains a 2.4 GHz RF transceiver, compliant with BLE 5.1 for wireless communication with any BLE-enabled device, such as a smartphone or a tablet, over a range of up to 9.5 m, close to the maximum range for class 2 Bluetooth connections (~10 m)[28]. Incoming wireless data buffers through I²C communication to the microcontroller on an event basis, such that communication and local control of the spatiotemporal patterns of haptic actuation remain decentralized. An additional NFC-based wireless tag, also connected via I²C with the microcontroller, provides low-power communication via contact tapping with NFC-enabled mobile devices or commercial NFC readers as the basis for activating the system.

Information exchanged with the haptic interface requires a structured communication protocol that encodes the configuration and/or operational parameters. The protocol described here involves firmware (device) and software (computer or handheld device)
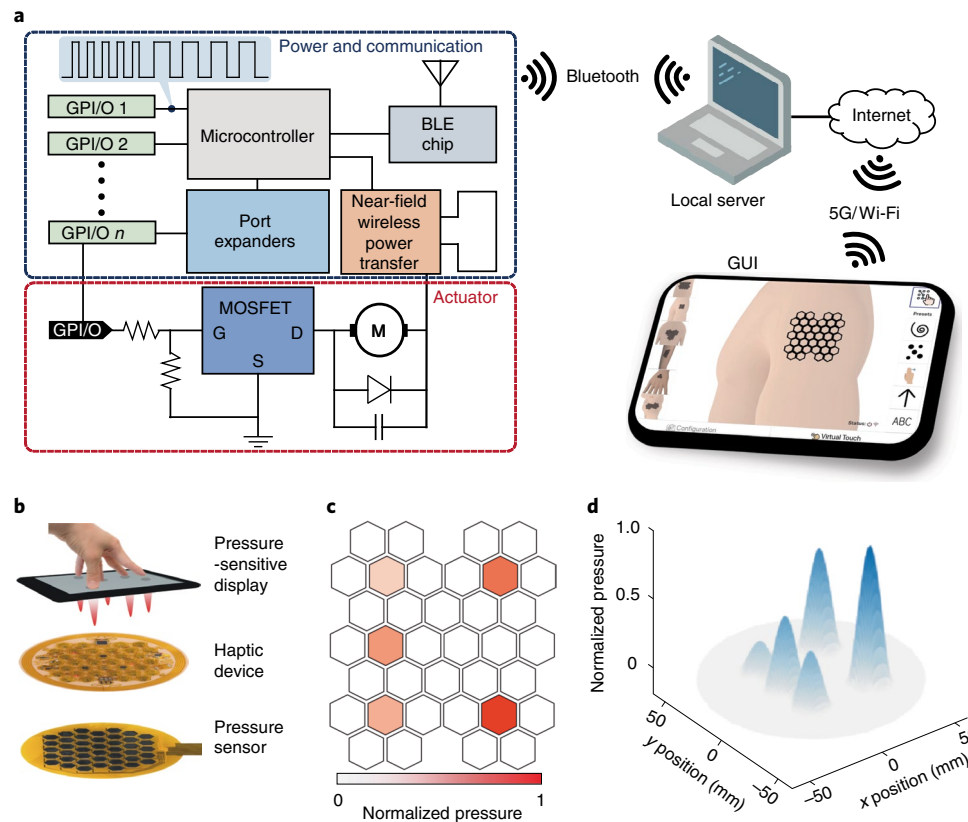
Fig. 2 | Operating principles. a, Circuit, block diagram and connection mechanisms of a haptic interface and its wireless interface to a touchscreen device. MOSFET, metal–oxide–semiconductor field-effect transistor; G, ground; S, source; D, drain; M, eccentric rotating mass motor. **b**, Photographs and diagrams to illustrate pressure-sensitive operation in which the haptic interface produces vibrations with intensities and spatial patterns matched to the distribution of pressure applied by the fingers onto a pressure-sensitive touchscreen. An array of pressure sensors to record the vibrational intensity from beneath to verify the operation. **c**, Spatial mapping of finger pressure recorded from the touchscreen device (namely, an iPhone X). **d**, Spatial mapping of pressure produced from the haptic interface and recorded from the array of the pressure sensor shown in **b**.

for intuitive, rapid and continuous interactions. Configuration commands include temporal information, such as frequency and duty cycles, to define the vibrational patterns for haptic actuation. Operational commands consist of instructions that represent vibrational modalities that the firmware in the microcontroller decodes and deploys to the actuator array. Five vibrational modalities are supported in this firmware based on ASK–PWM signals with user-programmable frequency and duty cycles (Supplementary Fig. 6). Three modalities initiate and terminate on a command basis (on/off commands), whereas the other two follow from programmed time parameters (single-pulse operation). As mentioned previously, the PWM defines the effective intensity of the sensation through control of the duty cycle. In this way, the device receives hybrid combinations of configurational and operational commands to achieve fast, spatiotemporal control, as demonstrated in subsequent sections.

As mentioned previously, a GUI supports intuitive, real-time engagement and it programmatically performs command encoding. The GUI, written in Python, is hosted in a local server with direct access to the haptic interface. This GUI can be accessed with a uniform resource locator using a Web browser on any touchscreen mobile computer to allow manipulation from any place in the world where there is a connection to the Internet. Figure 1d (and Fig. 2a, right) presents an example where the user manipulates one of the interfaces on a laptop computer with a touchscreen (for example, Surface Pro, Microsoft) connected to the Internet over a Wi-Fi network. The GUI also provides capabilities for configuring individual

actuators, including the frequency and duty cycle of the PWM input that defines the intensity.

Pressure-sensitive touchscreens (for example, iPhone X, Apple)[29] can convey not only the patterns of actuation but also the levels of intensity. Here the GUI encodes and delivers that information directly to the device such that haptic engagement with the user matches the spatial and temporal distributions of pressure applied by the fingers to the touchscreen. Figure 2b shows an example of detecting pressure-sensitive operations using a GUI running on an iPhone X, in which a user presses the touchscreen with five fingers, each with a different force. Figure 2c presents a spatial mapping of the force detected by the touchscreen across a scale of 1 to 400. The GUI encodes the pressure information into five levels defined by the PWM signal and sends the results to the haptic interface via Bluetooth. Figure 2d shows a mapping of the vibration intensity detected from a pressure sensor array that consists of 36 force-sensitive resistors that match the array geometry of the actuators in the haptic interface. The response time of the wireless haptic system, defined as the delay from the moment that the GUI detects a user input to the moment that an actuator starts vibrating, is 20 ms. Specifically, the time for the haptic interface to receive a Bluetooth wireless command is 17 ms and the time for the actuator to respond to that command is 3 ms (Supplementary Fig. 7a,b). The ERM requires a rise time of 30 ms to activate its maximum vertical displacement of 0.35 mm on the skin, but only 1 ms to reach the vibro-tactile sensory threshold of ~0.01 mm (ref. [30]). It is noteworthy that the times required to reach vertical displacements of 0.22

and 0.31 mm (63% and 90% of the maximum values) are 18 and 25 ms, respectively (Supplementary Fig. 7c,d). Adding the response time of the wireless system to the rise time of the ERM actuator results in a total response time of ~21–50 ms, corresponding to a virtual touch experience that is close to real time without perceptible delays[31]. The overall response time is shorter than any previously reported vibro-tactile haptic system, to the best of our knowledge (Supplementary Table 2).

Mechanisms of vibro-haptic actuation

The direct physical interface between the ERM actuators and skin leads to complex patterns of deformation and associated strong sensory perceptions, as improvements over the voice-coil-type actuators in previously described systems[23]. Quantitative study of these effects provides insights into the fundamental aspects of the resulting tactile sensations[30,32]. The measurements rely on a combination of optical approaches using particle tracking velocimetry (PTV) and three-dimensional (3D) digital image correlation (DIC) to yield the spatiotemporal maps of structural interactions between the actuators and surrounding skin at different vibrational intensities[33,34].

Figure 3 shows some results obtained from the skin of the inner forearm of a healthy male (30 years old), with additional measurements shown in Supplementary Videos 1 and 2. A high-pass eighth-order Butterworth filter and a 50 Hz cutoff frequency removes artefacts related to neuromuscular, cardiac and respiratory activities (Supplementary Fig. 8)[35]. Figure 3a presents a diagram of an ERM actuator on the skin, to highlight mechanisms that share certain characteristics of those found in an Euler's Disk—a spinning coin on a table[36]. Here, however, the actuator mainly rotates with respect to the z axis (Ω, the rotational speed) without spinning due to constraints that follow from its interface to the skin. The resulting unique vibrational motions increase in frequency ($f_0 = 1/\Omega$) and in amplitude along the lateral (Δx) and vertical (Δz) directions with increasing applied voltage (Supplementary Fig. 9a,b). Graphs in Figs. 3b,c present displacements at the centre of the actuator along the x and z axes, respectively. The precession-like motion leads to overall vertical displacements that are smaller than those in the lateral direction (Fig. 3c). Specifically, the peak-to-peak vertical and lateral displacements of an actuator on the skin operated at the maximum power of 158 mW (3.3 V voltage) are 0.23 and 0.86 mm, respectively. Figure 3d shows the lateral component of wave propagation along the skin induced by the operation of an actuator at a voltage of 3.3 V. As expected, the amplitude decreases with distance from the source, as the motions exhibit Rayleigh waves with velocities of ~12.5 mm s^{−1} (Supplementary Fig. 10), consistent with the expectation based on the mechanical properties of the skin (Supplementary Note 1). Figure 3e,f presents the maximum lateral and vertical displacements along the x axis, respectively[37]. The lateral and vertical amplitudes decrease by more than 90% and 40%, respectively, across a distance corresponding to the pitch of the actuators in the array (13 mm). These decays follow from the dynamics near and underneath the actuator and from propagating Rayleigh waves, the latter of which dominate at larger distances. As a result, the vertical magnitude is approximately twice that of the lateral magnitude at the pitch distance, consistent with the prediction for an incompressible solid with ν (Poisson's ratio) $= 0.5$ (ref. [38]). Figure 3g exhibits the 3D vertical-displacement contours at representative instants as a single ERM actuator placed on human skin vibrates. Figure 3h shows the contours at representative instants as a single ERM actuator embedded in the haptic system vibrates, measured on a slab of skin phantom. As observed in both cases, the precession-like motions induce self-similar 'swirly' motions on the skin and on the phantom. In particular, the spatial mapping results (Fig. 3h) show negligible crosstalk in the actual system across the array. The maximum displacement in the vicinity of an operating

ERM actuator decreases by more than 60% at the location of an adjacent actuator. The combined horizontal and vertical components of the vibration (Fig. 3g,h) provide sensations on the skin in the measured frequency range (70–130 Hz) that follow from the activation of both Meissner and Pacinian corpuscles. Quantitative comparisons of the performance of the ERM actuators with other types of actuator, including linear resonant actuators, piezoelectric actuators and voice-coil actuators, at a fixed power and over similar areas on human skin are shown in Supplementary Fig. 11 and Supplementary Videos 3 and 4 (Supplementary Note 2 provides details of the experimental procedures). The results indicate that the vertical displacements induced by the ERM exceed others by a substantial factor. The ERM also induces shear forces, through its Euler's disk–like rotational motion, not found in other actuators. These large, combined deformations create robust sensations even across areas of the skin where mechanoreceptors are scarce[15]. Based on qualitative assessments, most users experience a much stronger sense of perception through these mechanisms than those associated with the previously reported system, for a similar input power[23]. These large-area, densely packed arrays of ERM actuators can deliver diverse patterns of sensation, across a range of regions of the skin with different two-point discrimination thresholds (Supplementary Fig. 12). Examples include approximate reproductions of patterns that correspond to pinching, squeezing, rubbing and sliding (Supplementary Fig. 13 and Supplementary Video 5).

Assembly techniques for large-area, custom haptic interfaces

The ability to assemble haptic interfaces with different shapes, sizes and configurations via prefabricated building blocks represents an important aspect of the technology introduced here. Stitching these blocks together can yield large arrays (Fig. 4a), as illustrated for the case of a system with 49 islands and in a long, narrow layout designed for mounting along the length of the lower arm. The assembly uses board-to-board connectors for mechanical and electrical connections (Fig. 4a, inset). Any such system includes at least one control block (Fig. 4b) that consists of an array of seven actuators along with circuits for power management, wireless communication and control. Each of the other expandable blocks (Fig. 4c) consists of an array of seven actuators and a port expander IC with an I²C-based addressing capability of up to 32 addresses, for a maximum of 231 actuators (1 control and 32 expandable blocks) in a single system. Figure 4d,e presents circuit and block diagrams that describe the operational organization of the control and expandable blocks, respectively, where a control block is responsible for providing serial communication and supplying power to the expandable block via the connectors held by serpentine structures. Attaching batteries and a charging coil to the control block, typically located at a corner of the haptic interface, followed by encapsulation using layers of silicone completes the fabrication. Figure 4f–i shows five different designs created using this scheme. The smallest interface has 21 actuators (one control and two expandable blocks), in a shape designed for attachment onto the dorsal side of the hand (Fig. 4f, right). The long, narrow design (Fig. 4f, left) uses the board (49 actuators; one control and six expandable blocks) presented in Fig. 4a. The largest system incorporates 147 actuators (1 control and 20 expandable blocks), configured to naturally fit over the upper back (Fig. 4g). The layout shown in Fig. 4h (126 actuators; 1 control and 17 expandable blocks) is for the abdomen or the lumbar region. An additional example (98 actuators; 1 control and 13 expandable blocks) (Fig. 4i) is for mounting over the shoulder.

The skin-attachable module offers a simple sticker-like attachment process, thereby eliminating the need for separate straps, tapes, bands or other accessories required by many conventional haptic systems. Its disadvantages include (1) irritation that can occur as the device is peeled from the skin, (2) moisture that can accumulate
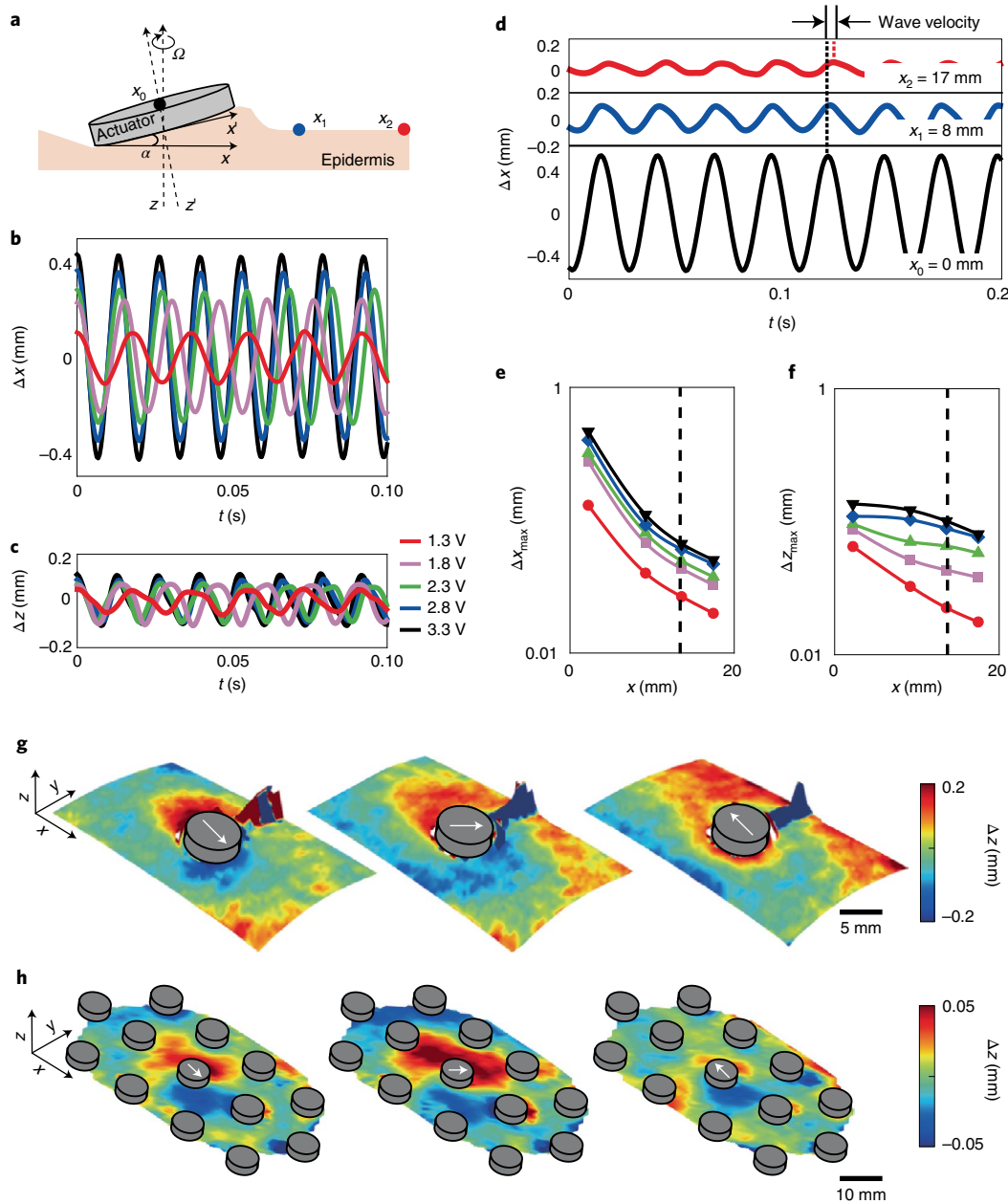
Fig. 3 | Mechanics of vibrational coupling to the skin. a, Free-body diagram of an ERM actuator on the skin. **b,c**, Lateral (**b**) and vertical (**c**) displacements at the centre of the actuator for different intensity settings. **d**, Lateral component of wave propagation along the skin. **e,f**, Maximum amplitudes of lateral (**e**) and vertical (**f**) components along the skin; the vertical dotted line indicates the distance of a unit cell (13 mm). **g,h**, Three-dimensional vertical-displacement contours at representative instants when the actuator tilts down in the +x (left), +y (middle) and –x (right) directions measured on human skin with a single ERM actuator (**g**) and on a skin phantom with the haptic interface (an array of ERM actuators) (**h**).

at the surface of the skin due to the presence of the device and (3) reduction in adhesive strength that can follow from heavy sweating. As an alternative, multiple haptic interfaces of the type described above can be mounted on stretchable fabrics (Spandex; polyether–polyurea co-polymer) to yield a robust, compression-based means for reversible mechanical coupling to the skin. Figure 4j shows multiple devices (total of eleven) with six different designs (Fig. 1a shows one design and Fig. 4f–i shows the remaining four designs), attached on the inner side of a shirt formed with such a fabric using hook-and-loop fasteners (Supplementary Fig. 14). A single donning process delivers multiple haptic interfaces to the skin, without the need for skin adhesives.

Navigation using haptic information interfaces

These systems can produce complex patterns of sensory inputs as functional channels of information. A simple illustration, suggested previously using comparatively primitive hardware[39], provides directions for the purposes of navigation. Here information passes wirelessly to the haptic interface from a global positioning system (GPS)-enabled navigation application on a smartphone to enhance awareness for pedestrians, joggers, bicyclists, motorcyclists and others via hands-free instructions that do not require attention to audio or video inputs. The example shown in Fig. 5a includes a haptic interface to the upper arm through a stretchable fabric band similar to the scheme described previously. The system can transmit
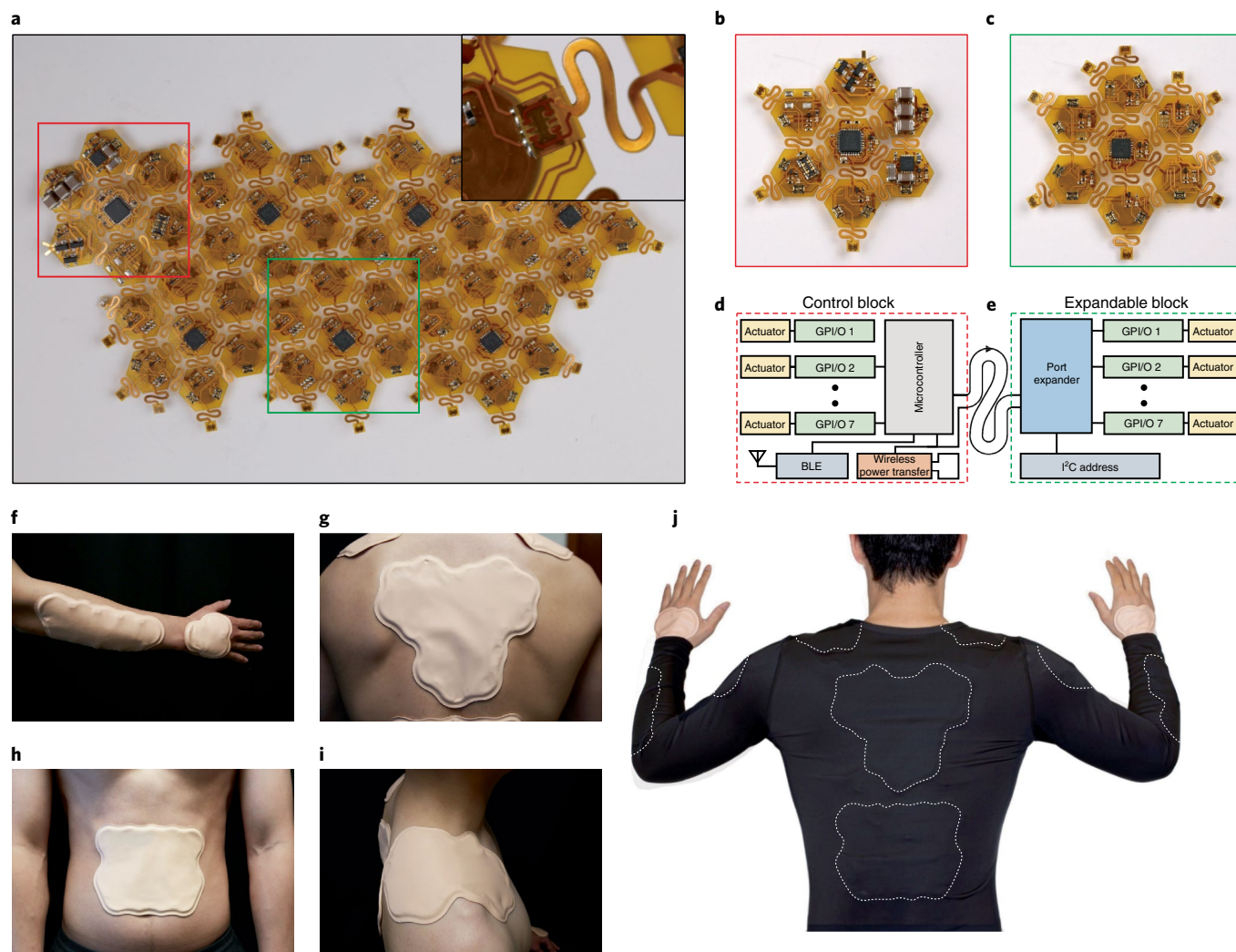
Fig. 4 | Assembly of haptic interfaces via prefabricated building blocks. a, Photograph of an array of haptic actuators assembled using prefabricated versions of one control block and seven expandable blocks. Each prefabricated block consists of seven actuators attached to hexagonal islands that interconnect through serpentine electrical traces. The assembly involves connecting the blocks using board-to-board connectors. The inset shows a magnified view of the connection point. **b**, Photograph of a control block, which consists of a microcontroller, wireless communication unit, power management unit and set of actuators. **c**, Photograph of an expandable block, which includes a port expander and a set of actuators. **d,e**, Circuit, block diagram and connection mechanisms of the control block (**d**) and expandable block (**e**). **f–i**, Photographs of haptic interfaces fabricated through the assembly of prefabricated blocks in layouts for the dorsal side of the hand and lower arm (**f**), upper back (**g**), abdomen (**h**) and shoulder (**i**). **j**, Haptic interfaces with different designs attached to the inner side of a Spandex-based compression shirt using hook-and-loop fasteners.

17 different preprogrammed spatiotemporal patterns of actuation to the skin, including 16 patterns that convey direction information and 1 pattern that signals 'arrived at destination'. Figure 5b shows a representative collection of four such patterns for direction. Here the light-emitting diodes (LEDs) serve as visual indicators of haptic points of engagement. Specifically, when the navigation system prompts a hard turn to the right (90° turn), the interface produces a haptic pattern of a rightwards arrow, first drawing a straight line sequentially from the left to right, followed by the head of the arrow from the right centre to the top and bottom together, in sequence. The arrow patterns produced at 45° either leftwards or rightwards in a similar sequential manner represent soft turns. Other patterns include a sequential arrow that starts from the bottom to top and a sequential pattern that expands from the periphery to the centre as a representation of 'go straight' and 'arrived at destination', respectively. Perception tests with five users (Supplementary Fig. 15) indicate that directions conveyed by 17 haptic patterns can be identified with an average accuracy of 85.4%. For enhanced accuracy in

turn-by-turn guidance, all arrow-based patterns include periods of vibration to indicate the distance between the user to the next point where the direction changes. For distances of less than 50, 30 and 15 m, the patterns follow a time period of 10, 7 and 3 s, respectively. The 'arrived at destination' pattern modulates the actuators with a period of 2 s as an abrupt sensation. Tests consisting of road guidance only using haptic feedback with ten different participants indicate a high degree of effectiveness in navigation using this haptic feedback approach. All the participants reached a destination that involved nine turns over a 0.5 mile walking distance, with an average time of 10 min and 14 s, close to the time (9 min) estimated by the navigation application (Apple Maps, Apple) but without audio or video inputs (Fig. 5c).

Haptic 'movies' to accompany music
A different application exploits these systems to enhance the experience of listening to music based on the fast processing of data passed wirelessly to the device by a microphone, as a real-time,
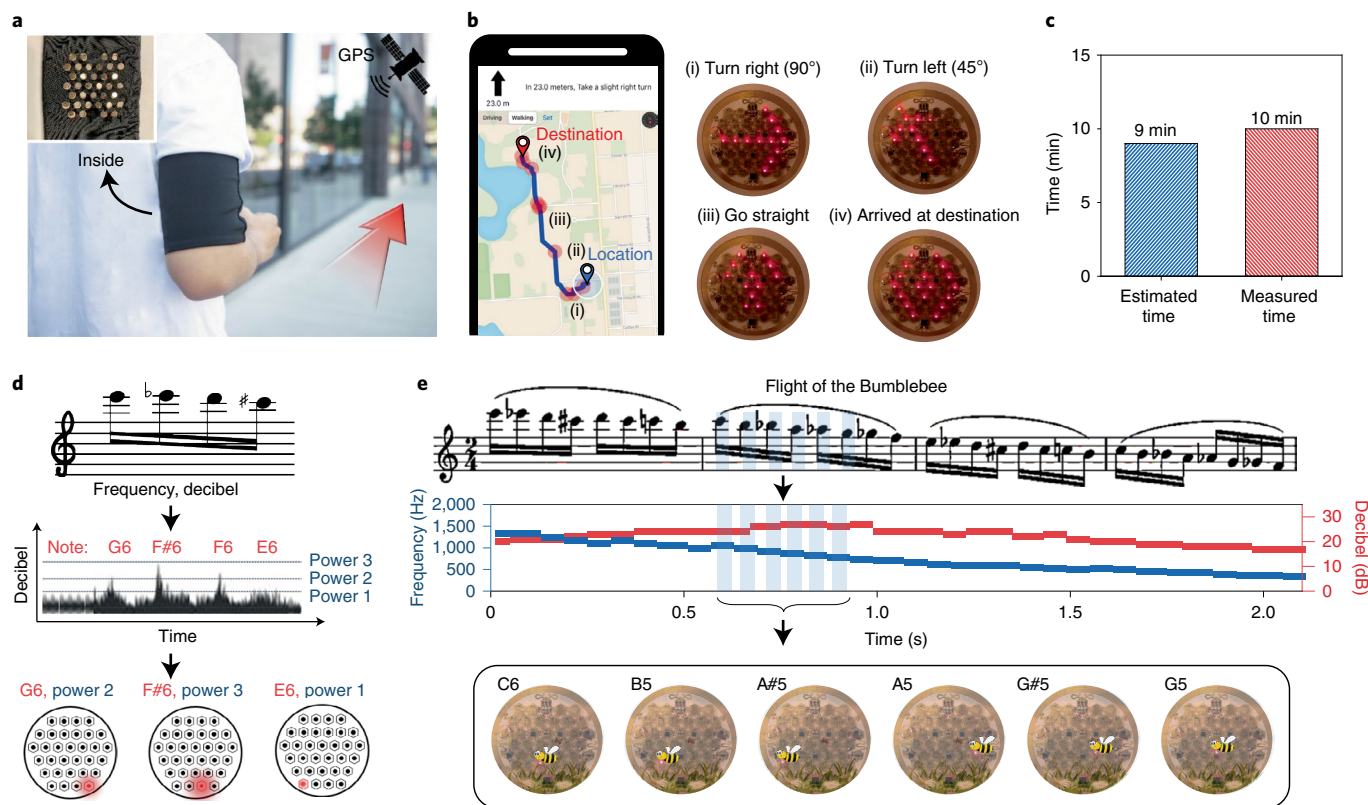
Fig. 5 | Delivery of visual and auditory information through spatiotemporal pattern of haptic actuation. a, Photograph of a GPS-based haptic navigation system that uses a haptic interface integrated in an armband. The inset shows the inner side of the armband where only the actuators are exposed. **b**, Image of a walking route (0.5 miles) based on a GPS-enabled navigation application of a smartphone. The nine red circles in the display represent the locations that require navigation instructions (that is, direction changes or arrived at destination). The right-side images show four examples (turn right (90°), turn left (45°), go straight and arrived at destination) of haptic patterns that the interface produces on the arm as the user reaches the corresponding locations in the route. The red LEDs on the haptic interface provide a visual indication of the powered actuators. **c**, Estimated time based on the navigation application shown in **b** and the actual measured time to reach the destination using haptic feedback as the instructions, without any audio or video inputs. **d**, Schematic illustration of a process for translating music into haptic representations, where both musical notes and decibel levels of the sound measured using a microphone translate in real time into commands that wirelessly control the haptic interface. Here each musical note is assigned to a single actuator of the array. The measured decibel level determines one of the three intensities of actuation. **e**, Musical notes of 'Flight of the Bumblebee' by Nikolai Rimsky-Korsakov and results of the real-time analysis of the frequency and decibel level of the sound.

sophisticated implementation of the notion of vibrational accompaniments[40]. Figure 5d illustrates this concept implemented using a haptic interface with 36 actuators, where the output of a microphone transforms into digital commands that assign individual musical notes to different actuators. Specifically, notes with increasing frequency map to the haptic interface starting from one corner of the array in an ascending order. The system covers up to full three octaves (12 notes each) at a maximum tempo of 216 bpm, limited by the speed of the BLE link and the number of actuators. Users can also distinguish diverse musical tempos such as 216, 170, 120 and 60 bpm with an average accuracy of 89.5% by recognizing the intervals in the haptic pattern (Supplementary Fig. 16). Figure 5e shows the haptic input associated with a musical score ('Flight of the Bumblebee' by Nikolai Rimsky-Korsakov) that includes a wide range of notes (three octaves) and a fast tempo (152 bpm). Here the top-leftmost actuator starts with a G# note of octave 3 and increases from left to right and towards the bottom-rightmost corner, which ends with a G note of octave 6. The intensity of haptic feedback corresponds, in four steps, to the decibel level for each note. At this tempo, the system has an accuracy rate of 90.7% in successfully translating the musical notes into haptic notes. The success rate increases to 95.3% as the tempo decreases to 136 bpm, and reaches 100% at 121 bpm. The errors probably arise from delays in

wireless packet delivery. In addition to musical notes, the interface can be used to translate speech, such as the English alphabet, into haptic form (Supplementary Fig. 17). Even this relatively small haptic interface provides over 68 billion (2^{36}) possible patterns, which increases to 4^{36} when operated in a combined manner with four levels of intensity. The system can, therefore, offer not only simple one-to-one mapping of notes or letters to haptic actuation (as demonstrated here) but also abstract complex spatiotemporal patterns that might derive from various qualitative, emotional features of music or speech. As a simple example, the actuators can simulate the Flight of the Bumblebee in the haptic form to accompany the score. Snapshots of a rendered cartoon video of a bumblebee flying over flowers is shown in Fig. 5e (bottom), where the positions change in a manner that corresponds to the music. A video representation of the track played using the haptic interface as well as the rendered cartoon video appears in Supplementary Video 6, where LED indicators serve visualization purposes.

Sensory replacement using a haptic interface

For amputees, haptics can form a type of sensory replacement as feedback for the control of robotic prosthetic interfaces[41,42]. Previous attempts in this context have failed to address key requirements due to limitations in the number of vibro-tactile actuators, speed of
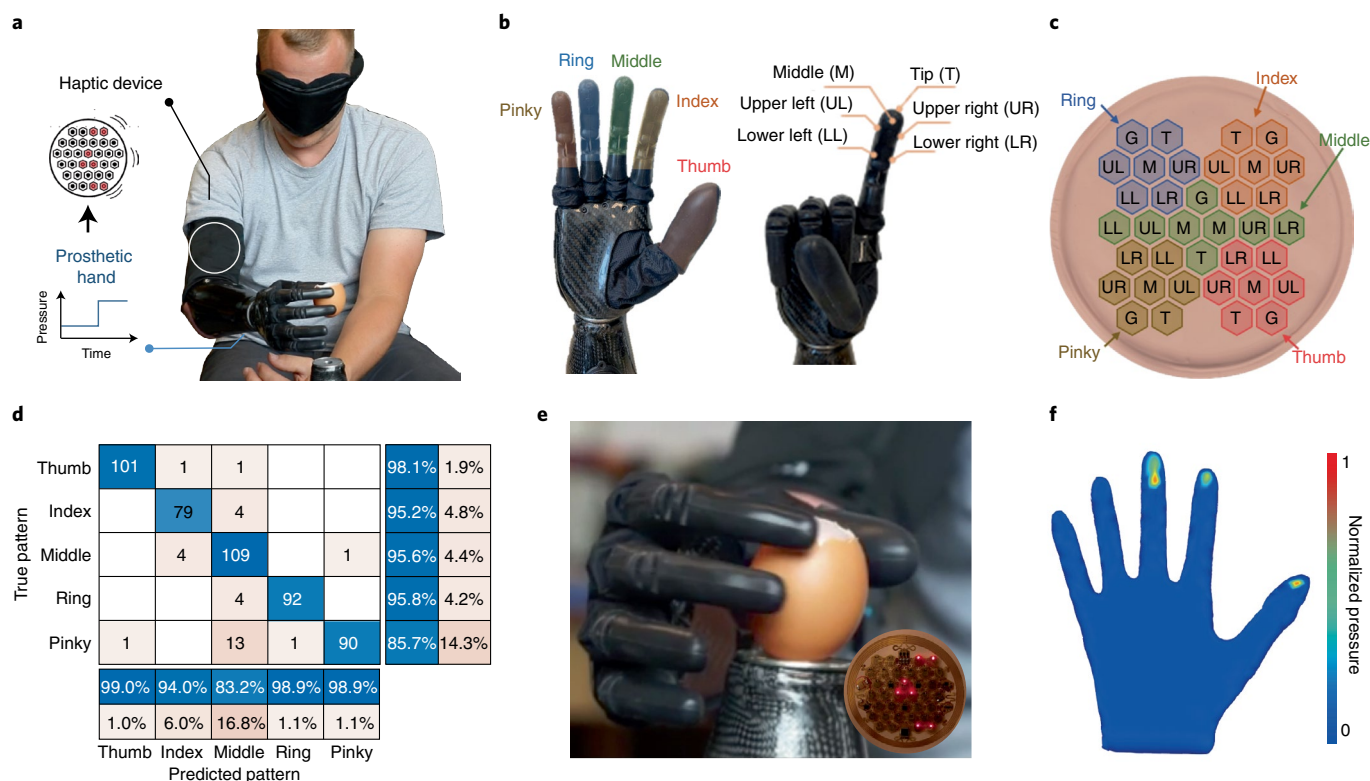
Fig. 6 | Sensory replacement with a haptic interface as feedback for control of a robotic hand. a, Photograph and schematic of the sensory replacement process. A haptic interface attached to the upper arm of an amputee produces vibration patterns that correspond to the distributions of pressure recorded from sensors on the fingers of a robotic prosthetic hand. **b**, Photograph of the prosthetic hand with illustrations that show the locations of pressure sensors in the fingers. In total, the system includes 30 resistive-type pressure sensors, with six sensors in each finger that are attached to the middle, tip, upper-left, upper-right, lower-left and lower-right positions across the ventral and lateral sides of the distal and intermediate phalanges. **c**, Photograph and schematic illustration of the map of actuators on the haptic interface for the 30 pressure sensors, where each actuator corresponds to a position in the fingers of the prosthetic hand. G, guide. **d**, Confusion matrix result of 100 blind perception tests for finger stimuli recognition using vibration patterns. **e**, Photograph of a prosthetic hand grasping an eggshell with haptic feedback on the upper arm. The inset shows the vibration pattern of the haptic interface during this process. **f**, Spatial distribution of pressure recorded from the sensors of the prosthetic hand.

control electronics and physical characteristics of the hardware. The technology introduced here creates many opportunities in this context, owing to the ability for large arrays to deliver complex tactile patterns at high speed, guided by external sensor inputs mounted on a prosthetic. Figure 6a shows a skin-integrated haptic interface on the upper arm of a human subject (44 years old) with lower-arm amputation who uses a robotic, prosthetic hand to grasp objects. Control over the fingers in the hand follow from electromyography signals measured from the upper arm. Here the pressure information generated by a distributed collection of sensors across the robotic fingers defines the physical nature of contact with an object, as wireless signals to determine control parameters for the haptic interface. Thus, the amputee can indirectly sense the tactile experience of contact through the intensities and patterns of sensation to facilitate control over the finger movement through electromyography signals. Specifically, the haptic interface produces a representation of the pattern of grasping force based on measurements from 30 pressure sensors placed at the fingertips and distributed along the ventral and lateral sides of the distal and intermediate phalanges of the robotic hand (Fig. 6b). The pressure data wirelessly pass to the haptic interface using Bluetooth protocols. The output of each sensor maps to an individual actuator in the haptic interface, in a way that resembles the anatomy of the hand to facilitate training and intuitive pattern recognition. For instance, operation of the array of seven actuators located at the bottom-left corner of the interface depends on measurements from sensors of the pinky finger of the prosthetic

hand. Similarly, the top-right, top-left, middle and bottom regions correspond to sensors of the ring finger, index finger, middle finger and the thumb of the prosthetic hand, respectively (Fig. 6c).

A training period includes the display of vibrations corresponding to pressure at preprogrammed finger positions, such as the ventral and lateral sides of the distal and intermediate phalanges of each fingertip (thumb and index, middle, ring and pinky fingers) in a random order every 5 s using the GUI controller, followed by user prediction and ground-truth identification (Supplementary Video 7). Training involves five users, each presented with 30 sequences of patterns and verbally informed with the corresponding position. Each sequence initially delivers a pattern that specifies the finger (thumb or index, middle, ring or pinky fingers), followed by a 300 ms pause and a pattern that specifies the position within the finger. The guide patterns for the thumb and index, ring and pinky fingers lie at the periphery of the actuator array and that for the middle finger lies in the middle of the array. This scheme facilitates training by matching with the anatomical positions (Fig. 6c). The delivery of 300 sequences of patterns in random order follows, with the verbal identification of the delivered position. The results of the perception tests on 100 sequences indicate that the average prediction accuracy among the 30 different points is 74.2% after training (Supplementary Fig. 18). The average prediction accuracy for distinguishing the finger positions is 94.8% (Fig. 6d).

Practical tests focus on grasping an eggshell without breaking the shell (Fig. 6e), both with and without haptic feedback. Figure 6f

shows a map of pressure distributions across the hand as the subject grasps an eggshell, indicating maximum pressures across the ventral side of the middle finger. Subsequently, the haptic interface generates a pattern of feedback that represents the map, such that the subject feels the grasp of an eggshell with spatial detail. Without haptic feedback, the amputee breaks the eggshell on grasping, as a result of a grasp pressure of 16 kPa (Supplementary Video 8). With haptic feedback, the amputee continuously receives pressure information to enable successful grasping without breakage, through a controlled grasp pressure of 1.5 kPa (Supplementary Video 9).

Conclusions

We report a modular skin-integrated haptic interface system that supports real-time, high-resolution operation based on control signals derived from a range of sources, including direct GUI inputs and wireless sensor networks. The approach can potentially provide full-body coverage at densities that meet or exceed two-point discrimination thresholds at nearly all anatomical locations. It allows for complex representations to be imposed across the skin with high spatiotemporal fidelity, thereby supporting a broad collection of unusual applications. Our use of scalable assembly techniques, as well as the alignment of many aspects of the base technology with commercial components and manufacturing methods, increase the prospects for the translation of this technology to a number of settings.

Our platform complements those that focus on interfaces to the fingertips and/or the palm of the hand, and the co-integration of these two distinct types of technology could offer additional opportunities in sensory experiences. Further research can expand the modes of interaction with the skin to include the independent actuation of shear and surface normal vibrations, static displacements and even patterns of heating and cooling. The approach could form the starting point of an information channel based on touch in many emerging applications including virtual, augmented and mixed reality, providing a potential component for the so-called metaverse and for advanced human–machine interfaces[11,43]. Efforts to connect the responses elicited by these systems to the physiology, neuroscience and psychology of perception represent promising future directions.

Methods

Fabrication of electronics. A thin FPCB (W-1005ED-N4, Xinyang) formed with conductive tracks served as the basis for mechanical support and electrical interconnections for electronic components and actuators. The FPCB itself consisted of a layer of polyimide (20 μm thick) with patterned traces of copper (18 μm thick) on the top and bottom surfaces, each encapsulated with an insulating polyimide film (20 μm thick) using a layer of silicone adhesive (12 μm thick) in between. Each serpentine that connects the hexagonal islands is 700 μm wide, 2.6 mm in initial end-to-end length and 210° in arc angle, supporting two 200-μm-wide copper traces separated by 100 μm on both sides. Some serpentines support a single 500-μm-wide copper trace, specifically reserved for the main power supply and the electrical ground, which carry high currents. The passive components (resistors, capacitors and inductors), microcontroller (ATmega328P-MNR, Microchip Technology), BLE system on chip (CC2640R2FRSMT, Texas Instruments), antenna (2450AT18D0100, Johanson Technology), port expander (XRA1201PIL24-F, MaxLinear), full-bridge rectifier (BAS4002ARPPE6327HTSA1, Infineon Technologies), d.c.–d.c. converter (LM5166XDRCR, Texas Instruments) and 3.7 V lithium polymer battery charge management controller (MCP73831T-4ADI/OT, Microchip Technology) were bonded to the FPCB via a low-temperature reflow process with soldering paste (TS391LT, Chip Quik) and a heat gun (Aoyue Int866). Furthermore, 36 ERM actuators (C0720B003D, Jinlong Machinery & Electronics) were mounted on the FPCB with double-sided Kapton tape and electrically connected by soldering thin copper wires on the pads of the actuators. A separate small FPCB was mounted with an NFC IC (M24LR04E-R, STMicroelectronics) connected to the main FPCB using board-to-board connectors (BM25-4S/2-V and BM25-4P/2-V, Hirose Electric). A soft silicone material (Silbione RTV 4420, Elkem) mixed with 5% white and 3% flesh silicone dyes (Silc Pig, Smooth-On) formed the top and bottom encapsulation layers, respectively. The top and bottom aluminium moulds for compression moulding (95 °C oven for 20 min) of the top layer were formed using a three-axis milling machine (Modela Pro II MDX 540, Roland DGA).

The bottom encapsulation structure consisted of a 1.0-mm-thick layer formed by curing 16 g silicone material on a level surface overnight in a Petri dish (150.0 mm diameter, Fisher Scientific) followed by laser cutting to create 36 circular openings (7.5 mm diameter) using a CO_2 laser (Universal Laser Systems). To encapsulate the device, the top layer was placed on the top aluminium mould, the FPCB substrate (with electronic components and actuators) was located inside and the bottom encapsulation layer was bonded to the top layer using uncured silicone material in an orientation that aligned the actuators with the openings. The circular openings that surround each actuator were sealed to the bottom encapsulation layer using silicone glue to reinforce the bond between the circuit board and encapsulation. After curing for 12 h at room temperature, a custom die (112307, Millennium Die Group) cut away excess silicone material from the edges to define the final device outline.

Assembly of prefabricated modular blocks. Assembly of prefabricated building blocks for haptic interfaces with diverse designs began with the fabrication of the control blocks, each of which consisted of an FPCB mounted with a microcontroller, BLE system on chip, NFC-tag IC, full-bridge rectifier, d.c.–d.c. converter and seven ERM actuators, with part numbers described previously. Each expandable block included an FPCB mounted with a port expander and seven actuators. For both control and expandable blocks, receptacle-type board-to-board connectors (BM25-4S/2-V, Hirose Electric) soldered on the top layer of the FPCB inside the hexagonal islands and header-type board-to-board connectors (BM25-4P/2-V, Hirose Electric) soldered on the bottom layer at the periphery of the serpentine structures, allowed assembly by connecting the periphery of the serpentines of a block to the hexagonal islands of another block to form mechanical and electrical connections by gently pressing the header connector to the receptacle connector. Each expandable block was assigned with an I²C address by connecting V_{CC} (supply voltage), GND (ground), SDA (serial data line) or SCL (serial clock line) to three different pins (A0, A1 or A2) of the port expander using 0 Ω jumper resistors. The encapsulation layers were prepared using the procedures described above, with the exception of the bottom encapsulation layer, which in this case used an aluminium plate (50 × 50 cm²) with 3-cm-high aluminium borders on all the sides to produce a large-area silicone layer (1 mm thick). Each design used a matching custom die to define the final outline of the haptic interface.

Integration on stretchable fabrics. Several hooks (hook-and-loop tape, Velcro) were adhered to the top side of each haptic interface, sewed using threads and reinforced with a silicone elastomer adhesive (Silbione RTV 4420, Elkem). The loops were attached on the stretchable fabric (Spandex long-sleeve compression shirt, ATHILO) side with threads, at the locations of hooks of different haptic interfaces. A specific embodiment for navigation studies used an armband (phone armband sleeve, E Tronic) that consists of dual layers of stretchable fabric. Here the haptic interface was attached in between the dual layers with the actuators exposed through the holes towards the skin for direct contact. A silicone glue inserted in between the inner layer of the armband and the interface at the regions of encapsulation in between the actuators fixed the interface in place.

BLE protocols, software control and system power. An open-source front-end compiler (Svelte) provided a tab for connection configuration, actuator parameterization, manual-actuator fabric activation and preset-actuator fabric activation overlaid on the body models. The Web user interface made hypertext transfer protocol requests to a hypertext transfer protocol server that proxies to the publisher side of the socket of an asynchronous messaging library (ZeroMQ). On the subscriber side of the socket, one or more hosts passed messages to a BLE module embedded in the touchscreen smart device, where each host is responsible for sequencing messages. The battery bank was charged through wireless power harvesting using the embedded loop coil (13.56 MHz) by placing the device on top of a transmitter antenna (ISC.ANT100/100, FEIG Electronic). A battery-free embodiment operated inside the range (50 cm) of a transmitter antenna (ISC. ANT800/600, FEIG Electronic) connected to a long-range reader module (ISC. LRM2500, FEIG Electronic) that provided 8 W RF power.

PTV. PTV experiments for measuring the surface waves initiated by ERM actuators involved recordings from a high-speed camera (2,048 × 1,088 in resolution; HT-2000M, Emergent) with 35 mm imaging lenses (F1.4 manual focus; Kowa) and an inclination angle of 45° at a sampling rate of 2,200 fps. The process tracked ~7–11 fiducial points marked on the actuators and surrounding skin. For measurements of a single actuator, these points were placed at $x = 0, \pm 8, \pm 13$ and ± 17, where $x = 0$ is the centre of the actuator. The experiments were conducted at five intensity settings, namely, 1.3, 1.8, 2.3, 2.8 and 3.3 V, and recorded for ~22,000 image sets (~10 s) per case. For the array of three actuators, the points were marked at $x = 0, \pm 6.5, \pm 9.5$ and ± 13.0 (centre of adjacent actuators), as well as at $x = \pm 19.5$ and ± 22.5. The approach allowed the investigation of vibration dynamics with a spatial resolution of ~0.1 mm per pixel, tracking capability at the subpixel level, temporal resolution of <0.5 ms and investigation area that is substantially larger than the area of a single hexagonal pixel of the presented haptic interface (area, 146.4 mm²). Preprocessing, calibration, tracking and postprocessing used customized PTV codes. The image sequences were preprocessed by subtracting the

background noise and enhancing the contrast. Fiducial points were detected at the subpixel level, tracked using the Hungarian algorithm and linked by performing a five-frame gap closing to produce long trajectories. The displacement was filtered and computed using an eighth-order Butterworth filter (cutoff frequency, 50 Hz) and fourth-order B-splines. The enhanced image sequence was magnified using the Eulerian video magnification method[44].

3D DIC. Two sets of 3D DIC experiments defined the 3D deformations of (1) the surrounding skin modulated by a single ERM actuator and (2) a skin phantom modulated by an ERM actuator embedded in a haptic interface system. The 3D displacements were captured by two of the same high-speed cameras used in the PTV experiments and processed using the open-source 3D DIC software, namely, MultiDIC[34]. For the first experiment, the actuator and surrounding skin were uniformly coated with black speckles by spray painting the skin surface and measuring at a sampling rate of 1,000 fps for the case of a single ERM operating at 3.3 V. For the second experiment, 3D deformations induced by the haptic device were measured by placing a slab of 3-mm-thick transparent silicone elastomer (polydimethylsiloxane; 20:1, SYLGARD 184, Dow Corning) on the actuator-exposed side of the haptic interface at a sampling rate of 700 fps. The investigation volume was $45 \times 30 \times 10\,mm^3$, and the root mean square error of 3D reconstruction was ~50 μm for both experiments. To achieve high-resolution, accurate wave-displacement characteristics, the DIC subset radius and spacing were set at 16 and 8 pixels, respectively, resolving over 2,000 grids.

Providing navigation commands via a haptic interface. The haptic-based navigation demonstration used a navigation and Bluetooth communication system developed through the Swift software program (Apple). The location of the user was updated once per second using GPS, and the route and walking/driving time to the destination were calculated using traffic information provided by a smartphone-based application (Apple Maps, Apple). Turn-by-turn information was transmitted to the haptic device using Bluetooth communication to provide information on direction and distance through the spatiotemporal patterns of vibro-haptic engagement. For displaying the dynamic patterns of information, actuators flashed one by one in time sequence, with turn-on and turn-off time intervals of 100 ms (Supplementary Fig. 19). The dynamic pattern of actuation was repeated every 10, 7 and 3 s for remaining distances of 50, 30 and 15 m, respectively.

Translating music into haptic 'movies'. The operation of the musical system with haptic engagement involved the collection of sound information through the microphone of a mobile control module (iPhone X, Apple) and the analysis of frequency and decibel content in real time using the fast Fourier transform method. This information was passed to the haptic interface through Bluetooth communication, in the form of commands to actuate the spatiotemporal patterns of vibro-haptic actuation corresponding to notes, classified into 36 different categories depending on the frequency. The decibel level of the notes defined the amplitude of actuation. Specifically, the bias applied to the actuator was controlled using PWM, with duty cycles of 40%, 60%, 80% and 100% corresponding to decibel levels of 10, 20, 30 and 40 dB, respectively. For sounds above 40 dB, an 'X'-shaped pattern of vibration was activated as an alert notification.

Human-participant tests for accuracy measurements. Five healthy adult volunteers (age, 28–40 years; male individuals) performed the tests for two-point discrimination and accuracy measurements via a haptic interface with no additional human-participant risk, following the provided study guidelines. The experimental protocols for the on-body studies were approved by the Institutional Review Board of Northwestern University (IRB#: STU00214661), and all the participants provided their consent before the test.

Providing haptic feedback to an amputee for control of a robotic prosthetic. Demonstrations used a robotic prosthetic hand (Ability Hand, PSYONIC) that contains 30 force-sensitive resistor-based pressure sensors with a Bluetooth interface to the haptic interface. Motions of the fingers of the hand were controlled through the electromyography data acquired from the upper arm. The measured pressures, across a range of 0 to 4,095 in arbitrary units (a.u.), were converted to vibration intensities through control of the duty cycle of PWM, where 40%, 60%, 80% and 100% corresponded to pressures of 300, 600, 1,200 and 2,400 a.u., respectively. The positions of the pressure sensors and associated actuators in the haptic interface were matched in a manner shown in Fig. 6c. A volunteer with lower-arm amputation (age, 44 years; male individual) performed sensory replacement feedback for control of robotic prosthetics with no additional human-participant risk, following the provided study guidelines. The experimental protocols were approved by the Institutional Review Board of the University of Illinois at Urbana-Champaign (IRB#: 13920) and the amputee provided his consent before the test. Blind tests for perception involved covering the eyes of the amputee followed by a random activation of the haptic interface with one of the five patterns shown in Fig. 6c. The finger that was stimulated was compared with the finger determined by the amputee based on haptic feedback. Blind perception tests based on 100 random stimuli were conducted before training, after 10 min of training and after 20 min of training.

References
1. Okamura, A. M. Haptic feedback in robot-assisted minimally invasive surgery. *Curr. Opin. Urol.* **19**, 102–107 (2009).
2. Jones, M. G., Minogue, J., Tretter, T. R., Negishi, A. & Taylor, R. Haptic augmentation of science instruction: does touch matter? *Sci. Edu.* **90**, 111–123 (2006).
3. Morris, D., Tan, H., Barbagli, F., Chang, T. & Salisbury, K. Haptic feedback enhances force skill learning. In *Second Joint EuroHaptics Conference and Symposium on Haptic Interfaces for Virtual Environment and Teleoperator Systems (WHC'07)* 21–26 (IEEE, 2007).
4. Bai, H., Li, S. & Shepherd, R. F. Elastomeric haptic devices for virtual and augmented reality. *Adv. Funct. Mater.* **31**, 2009364 (2021).
5. Shi, Y. et al. Self-powered electro-tactile system for virtual tactile experiences. *Sci. Adv.* **7**, eabe2943 (2021).
6. Yang, T. et al. Recent advances and opportunities of active materials for haptic technologies in virtual and augmented reality. *Adv. Funct. Mater.* **31**, 2008831 (2021).
7. Biswas, S. & Visell, Y. Emerging material technologies for haptics. *Adv. Mater. Technol.* **4**, 1900042 (2019).
8. Ankin, H. T. Y. K., Nirmal, A., Kulkarni, M. R., Accoto, D. & Mathews, N. Soft actuator materials for electrically driven haptic interfaces. *Adv. Intell. Syst.* **4**, 2100061 (2021).
9. Fan, R. E. et al. A haptic feedback system for lower-limb prostheses. *IEEE Trans. Neural Syst. Rehabil. Eng.* **16**, 270–277 (2008).
10. Holden, M. K. Virtual environments for motor rehabilitation: review. *Cyberpsychol. Behav.* **8**, 187–211 (2005).
11. Zhu, M. et al. Haptic-feedback smart glove as a creative human-machine interface (HMI) for virtual/augmented reality applications. *Sci. Adv.* **6**, eaaz8693 (2020).
12. HaptX. Haptic gloves for virtual reality and robotics. https://haptx.com/ (2021).
13. Bark, K. et al. Effects of vibrotactile feedback on human learning of arm motions. *IEEE Trans. Neural Syst. Rehabil. Eng.* **23**, 51–63 (2015).
14. Choi, S. & Kuchenbecker, K. J. Vibrotactile display: perception, technology, and applications. *Proc. IEEE* **101**, 2093–2104 (2013).
15. Jung, Y. H., Kim, J.-H. & Rogers, J. A. Skin-integrated vibrohaptic interfaces for virtual and augmented reality. *Adv. Funct. Mater.* **31**, 2008805 (2021).
16. Yin, J., Hinchet, R., Shea, H. & Majidi, C. Wearable soft technologies for haptic sensing and feedback. *Adv. Funct. Mater.* **31**, 2007428 (2021).
17. Wiliams, S. R. & Okamura, A. M. Body-mounted vibrotactile stimuli: simultaneous display of taps on the fingertips and forearm. *IEEE Trans. Haptics* **14**, 432–444 (2021).
18. Rotella, M., Guerin, K., He, X. & Okamura, A. M. HAPI bands: a haptic augmented posture interface. In *2012 IEEE Haptics Symposium* 163–170 (IEEE, 2012).
19. Kapur, P., Jensen, M., Buxbaum, L. J., Jax, S. A. & Kuchenbecker, K. J. Spatially distributed tactile feedback for kinesthetic motion guidance. In *2010 IEEE Haptics Symposium* 519–526 (IEEE, 2010).
20. Lindeman, R. W., Page, R., Yanagida, Y. & Sibert, J. L. Towards full-body haptic feedback: the design and deployment of a spatialized vibrotactile feedback system. In *Proc. ACM Symposium on Virtual Reality Software and Technology (VRST)* 146–149 (ACM, 2018).
21. bHaptics. Next generation full body haptic suit—bHaptics TactSuit. https://www.bhaptics.com/ (2021).
22. TESLASUIT. Full body haptic feedback and motion capture tracking VR suit. https://teslasuit.io/ (2021).
23. Yu, X. et al. Skin-integrated wireless haptic interfaces for virtual and augmented reality. *Nature* **575**, 473–479 (2019).
24. Mancini, F. et al. Whole-body mapping of spatial acuity for pain and touch. *Ann. Neurol.* **75**, 917–924 (2014).
25. Xu, S. et al. Soft microfluidic assemblies of sensors, circuits, and radios for the skin. *Science* **344**, 70–74 (2014).
26. Lee, K. et al. Mechano-acoustic sensing of physiological processes and body motions via a soft wireless device placed at the suprasternal notch. *Nat. Biomed. Eng.* **4**, 148–158 (2020).
27. The Electronic Code of Federal Regulations (e-CFR) Title 47, 1.1310. Radiofrequency radiation exposure limits. https://www.ecfr.gov/cgi-bin/retrieveECFR?gp=&SID=81a1c5a13f8d02f165a06af6937d612&mc=true&n=3pt47.1.1&r=PART&ty=HTML#se47.1.1_11310 (e-CFR, 2019).
28. Collotta, M., Pau, G., Talty, T. & Tonguz, O. K. Bluetooth 5: a concrete step forward toward the IOT. *IEEE Commun. Mag.* **56**, 125–131 (2018).

29. Apple Inc. Human interface guidelines—3D touch. https://developer.apple.com/design/human-interface-guidelines/ios/user-interaction/3d-touch/ (2021).

30. Johnson, K. O. The roles and functions of cutaneous mechanoreceptors. *Curr. Opin. Neurobiol.* **11**, 455–461 (2001).

31. Doxon, A. J., Johnson, D. E., Tan, H. Z. & Provancher, W. R. Human detection and discrimination of tactile repeatability, mechanical backlash, and temporal delay in a combined tactile-kinesthetic haptic display system. *IEEE Trans. Haptics* **6**, 453–463 (2013).

32. Shao, Y., Hayward, V. & Visell, Y. Spatial patterns of cutaneous vibration during whole-hand haptic interactions. *Proc. Natl Acad. Sci. USA* **113**, 4188–4193 (2016).

33. Jeong, H. et al. Differential cardiopulmonary monitoring system for artifact-canceled physiological tracking of athletes, workers, and COVID-19 patients. *Sci. Adv.* **7**, eabg3092 (2021).

34. Solav, D., Moerman, K. M., Jaeger, A. M., Genovese, K. & Herr, H. M. MultiDIC: an open-source toolbox for multi-view 3D digital image correlation. *IEEE Access* **6**, 30520–30535 (2018).

35. Joyce, G. C. & Rack, P. M. H. The effects of load and force on tremor at the normal human elbow joint. *J. Physiol.* **240**, 375–396 (1974).

36. Moffatt, H. K. Euler's disk and its finite-time singularity. *Nature* **404**, 833–834 (2000).

37. Royston, T. J. et al. Estimating material viscoelastic properties based on surface wave measurements: a comparison of techniques and modeling assumptions. *J. Acoust. Soc. Am.* **130**, 4126–4138 (2011).

38. Bedford, A. & Drumheller, D. *Elastic Wave Propagation* (John Wiley & Sons, 1994).

39. Kiss, F., Boldt, R., Pfleging, B. & Schneegass, S. Navigation systems for motorcyclists: exploring wearable tactile feedback for route guidance in the real world. In *Proc. 2018 CHI Conference on Human Factors in Computing Systems (CHI)* 617 (ACM, 2018).

40. Tanaka, A. & Parkinson, A. Haptic wave: a cross-modal interface for visually impaired audio producers. In *Proc. 2016 CHI Conference on Human Factors in Computing Systems (CHI)* 2150–2161 (ACM, 2016).

41. Fan, R. E. et al. Pilot testing of a haptic feedback rehabilitation system on a lower-limb amputee. In *2009 ICME International Conference on Complex Medical Engineering* 1–4 (IEEE, 2009).

42. Kim, K. & Colgate, J. E. Haptic feedback enhances grip force control of semg-controlled prosthetic hands in targeted reinnervation amputees. *IEEE Trans. Neural Syst. Rehabil. Eng.* **20**, 798–805 (2012).

43. Ko, S. H. & Rogers, J. A. Functional materials and devices for XR (VR/AR/MR) applications. *Adv. Funct. Mater.* **31**, 2106546 (2021).

44. Wu, H.-Y. et al. Eulerian video magnification for revealing subtle changes in the world. *ACM Trans. Graph.* **31**, 65 (2012).

Author contributions

Y.H.J. and J.A.R. conceived the idea, designed the research, analysed the data and wrote the manuscript. Y.H.J., J.-Y.Y., A.V.-G., J.-H.K., M.P., J.L. and C.-J.S. designed the device and carried out the fabrication. A.V.-G., R.S. and J.T. designed the operation protocols and GUI. J.-T.K., H.L. and R.A. performed the mechanical characterization and analysis. A.A. and J.C. designed and programmed the prosthetic hand. Y.H.J., J.-Y.Y, A.V.-G., J.-H.K., H.-S.S., C.-J.S., J.-K.C., D.S.Y., Y.P., H.R., H.-J.Y., G.L., H.J., J.U.K., T.-I.K. and Y.H. carried out the experimental validation and analysis.

Competing interests

The authors declare no competing interests.

Additional information

Supplementary information The online version contains supplementary material available at https://doi.org/10.1038/s41928-022-00765-3.

Correspondence and requests for materials should be addressed to John A. Rogers.

Peer review information *Nature Electronics* thanks Herbert Shea, Xiaoming Tao and the other, anonymous, reviewer(s) for their contribution to the peer review of this work.

Reprints and permissions information is available at www.nature.com/reprints.

Publisher's note Springer Nature remains neutral with regard to jurisdictional claims in published maps and institutional affiliations.